Supporting Information for

Incorporating Nanoscale Effects into a Continuum-Scale Reactive Transport Model for CO_2-Deteriorated Cement

Qingyun Li[1], Carl I. Steefel,[2] and Young-Shin Jun[1], *

[1]*Department of Energy, Environmental and Chemical Engineering,*

Washington University, St. Louis, MO 63130

[2]*Energy Geosciences Division, Lawrence Berkeley National Laboratory, Berkeley, CA 94720*

E-mail: ysjun@seas.wustl.edu

http://encl.engineering.wustl.edu/

Environmental Science and Technology

*To Whom Correspondence Should be Addressed

Summary

18 pages, including 2 Tables and 13 Figures.

S1. Description of the $CaCO_3$ Phase Comparison Experiments

To compare the $CaCO_3$ formed in the cement and in the brine, we did additional experiments to collect these $CaCO_3$ precipitates. After these experiments, the reactor was degassed for 20 min and precipitates were gently collected using a spatula from the brine, most of which were attached to the Teflon liner inside the stainless steel reactor wall. The rapid degassing rate was to minimize the formation of secondary precipitates during the process. For these additional experiments, cement samples were not analyzed because fast degassing may have caused artifacts. The precipitates were rinsed with ultrapure deionized water (DI water, resistance > 18 MΩ • cm) and dried with nitrogen gas. The precipitates collected from the 10-day system had a mass of ~ 0.2 g, much more than those collected from the 6-day system (0.02 g), as shown in Figure S1. This difference indicates that most of the precipitates were formed during the reaction rather than during degassing, because both the 6-day and 10-day system had similar degassing procedures. In addition, because $CaCO_3$ has several polymorphs and the rapid precipitation (i.e., high supersaturation) typically begins with amorphous $CaCO_3$,[1-3] we would not expect to have a good crystalline structure in the XRD spectra for the $CaCO_3$ collected in brine if they were quickly formed during the rapid degassing process. After these precipitates were fully dried, they were ground to powder for XRD characterization.

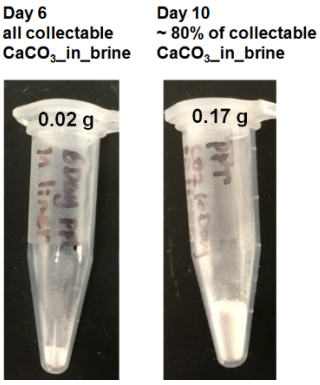

Figure S1. Amounts of $CaCO_3$ in brine collected from Day 6 and Day 10 systems for XRD analyses.

The cement samples were taken out of the reactor and rinsed with DI water, and then dried at ~50 ºC in an oven for ~ 5 hours. After the samples were dried, XRD sample powder was prepared from the carbonated layer. All these secondary precipitates were characterized to be a mixture of calcite and aragonite as shown in Figure 3.

S2. Calculation of Initial Cement Composition

The initial compositions of the cement grid cells were determined using XRF results reported in our previous study (Table S1).[4] Table S1 is reproduced with permission from [Qingyun Li, Yun Mook Lim, Katharine M. Flores, Kelly Kranjc, and Young-Shin Jun. Chemical Reactions of Portland Cement with Aqueous CO_2 and Their Impacts on Cement's Mechanical Properties under Geologic CO_2 Sequestration Conditions. *Environmental Science & Technology*, 2015, 49 (10), 5476-5483.] Copyright [2015] American Chemical Society.

Table S1. X-ray fluorescence analysis of cement before hydration. (From previous work by Li et al.)

	wt%
K_2O	0.2
CaO	53.8
TiO_2	0.16
MnO	0.05
Fe as Fe_2O_3	3.64
Fe as FeO	0.0
Na_2O	0.2
MgO	2.5
Al_2O_3	2.6
P_2O_5	0.10
SiO_2	19.0
Loss on ignition	19.0

Assuming 100 g of anhydrate cement powder, the calculated primary elemental components are 0.96 mole of Ca, 0.32 mole of Si, 0.004 mole of Fe, and 0.05 mol of Al. Distributing these elements to anhydrous products gives 0.17 mole of C_2S, 0.15 mole of C_2S, 0.05 mole of C_3A, and 0.004 mole of C_4AF. During the hydration of cement, the main components of Portland cement powder, alite ($3CaO\text{-}SiO_2$, or C_3S) and belite ($2CaO\text{-}SiO_2$, or C_2S), react with water to form C-S-H. The hydration reactions can be written as

$$C_3S + (1.4 + x)H = C_{1.6}SH_{x+1} + 1.4CH \text{ and} \quad \text{Eq. (S1)}$$

$$C_2S + (0.4 + x)H = C_{1.6}SH_x + 0.4CH\ . \quad \text{Eq. (S2)}$$

Considering only calcium silicates, the hydrated products from the hydration reaction are 0.32 mole of C-S-H and 0.30 mole of CH. Using reported densities for gel C-S-H and CH,[5] the calculated C-S-H and CH volumes are 27 and 10 cm^3, in which the CH volume occupies

about 14% of the total paste volume. Keeping the relative ratio of C-S-H to CH, the C-S-H occupies about 38% of the total volume. Because the cement pastes used in our studies were comparatively newly hardened, the initial composition of CH and porosity in the CrunchTope model was increased slightly to mimic our situation. The resulting initial composition used in our model is shown in Table 1 in the main text.

S3. Additional Results and Images

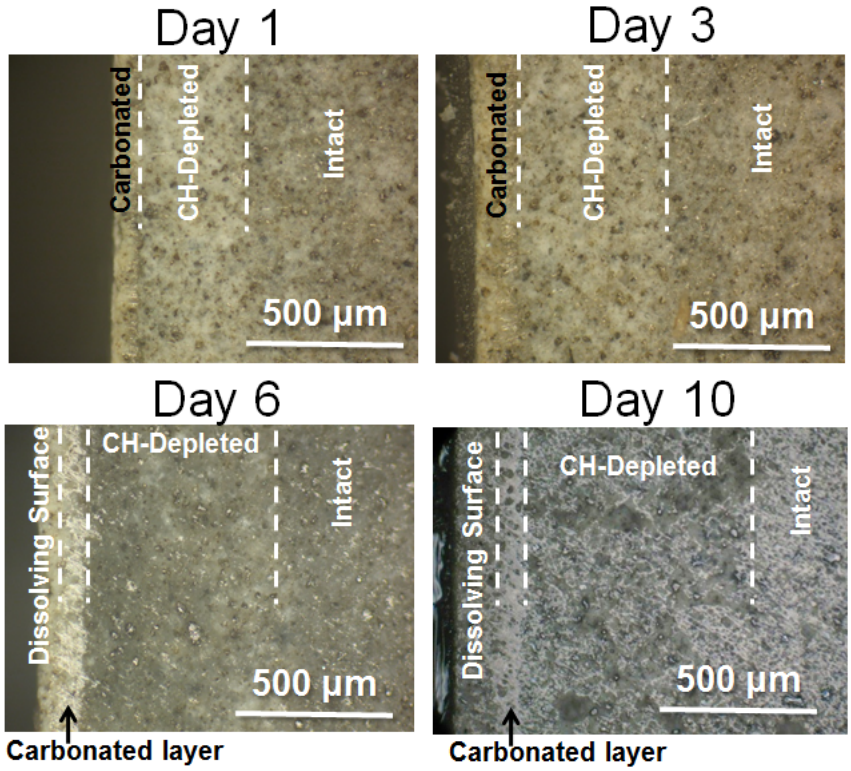

Figure S2 Optical images of reacted cement at Days 1, 3, 6, and 10. The image for Day 10 is adapted from Li et al. (2015).[4] Dotted lines indicate the interfaces between zones.

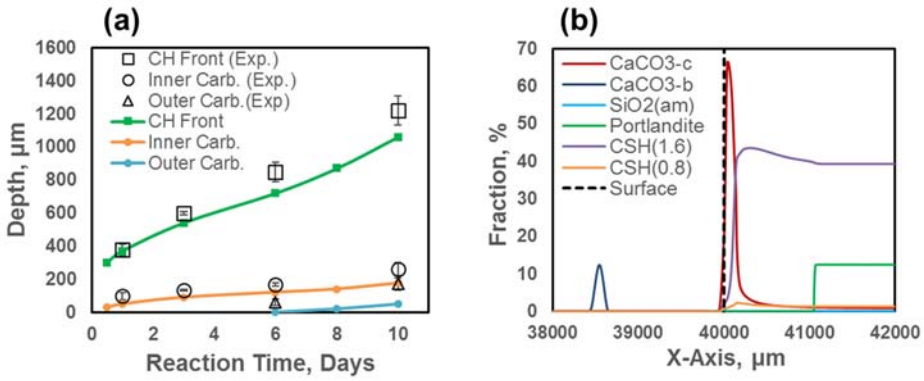

Figure S3 Modeling results with the ion-specific diffusion coefficients listed in Table S2. (a) Evolution of mineral fronts with respect to reaction days. (b) Mineral fraction at Day-10 of the reaction. Considering the uncertainty of the diffusivity estimations, the differences between these results and those predicted with a fixed diffusion coefficient (3×10^{-9} m^2/s) are not significant.

Table S2. Diffusion coefficient D_i estimated for individual ions.[6-9]

Species	D_i, $10^{-9}m^{-2}/s$
H^+	8.379
Ca^{2+}	0.714
OH^-	4.743
CO_3^{2-}	0.860
HCO_3^-	1.062
$CO_2(aq)$	1.719
Cl^-	1.809
Na^+	1.197
Other	3.000

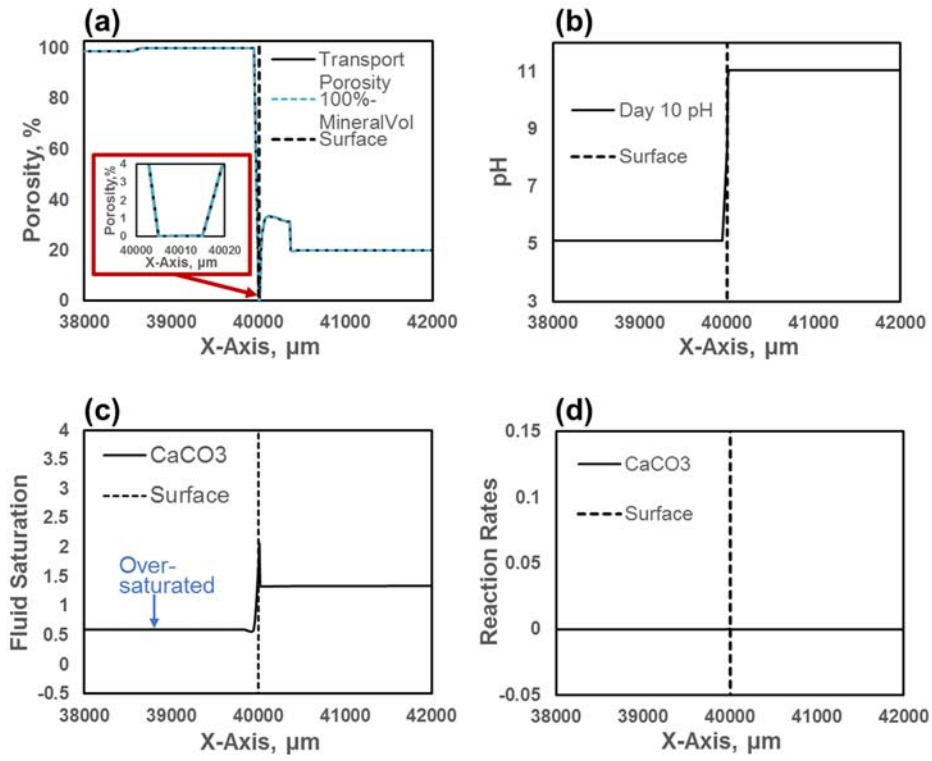

Figure S4 Simulation results for Day 10 without consideration of nanoscale mechanisms. (a) Porosity profile. The porosity for transport is the same as $1 - \sum_j \emptyset_{mj}$, and decreases to zero in the carbonated zone. (b) pH profile. (c) $CaCO_3$ saturation. The brine is oversaturated with respect to $CaCO_3$. (d) Reaction rates for $CaCO_3$. The cement is passivated and the reaction rates are zero throughout the domains.

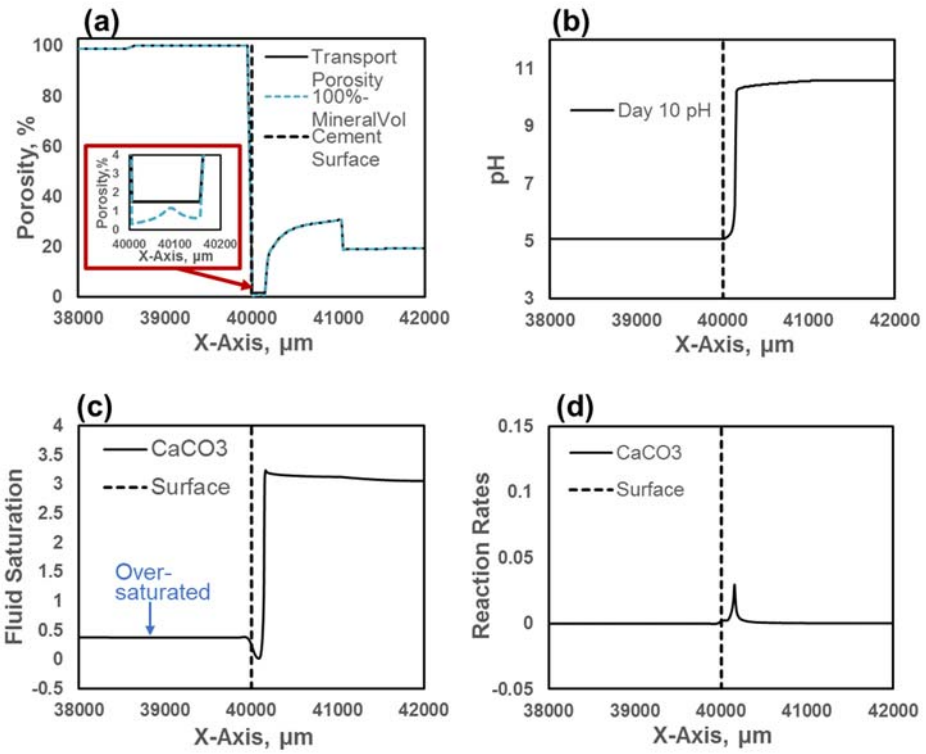

Figure S5 Simulation results for Day 10 with consideration of incomplete filling of nanopores. (a) Porosity profile. The porosity for transport is $\emptyset_{min}$ when $1 - \sum_j \emptyset_{mj} < \emptyset_{min}$, according to Eq. 5. This porosity allows diffusion of the acidic brine through the carbonated layer. (b) pH profile. (c) $CaCO_3$ saturation. The brine is oversaturated with respect to $CaCO_3$. (d) Reaction rates for $CaCO_3$. $CaCO_3$ is precipitating at the inner front of the carbonated layer, but is not dissolving at the outer front of the carbonate layer.

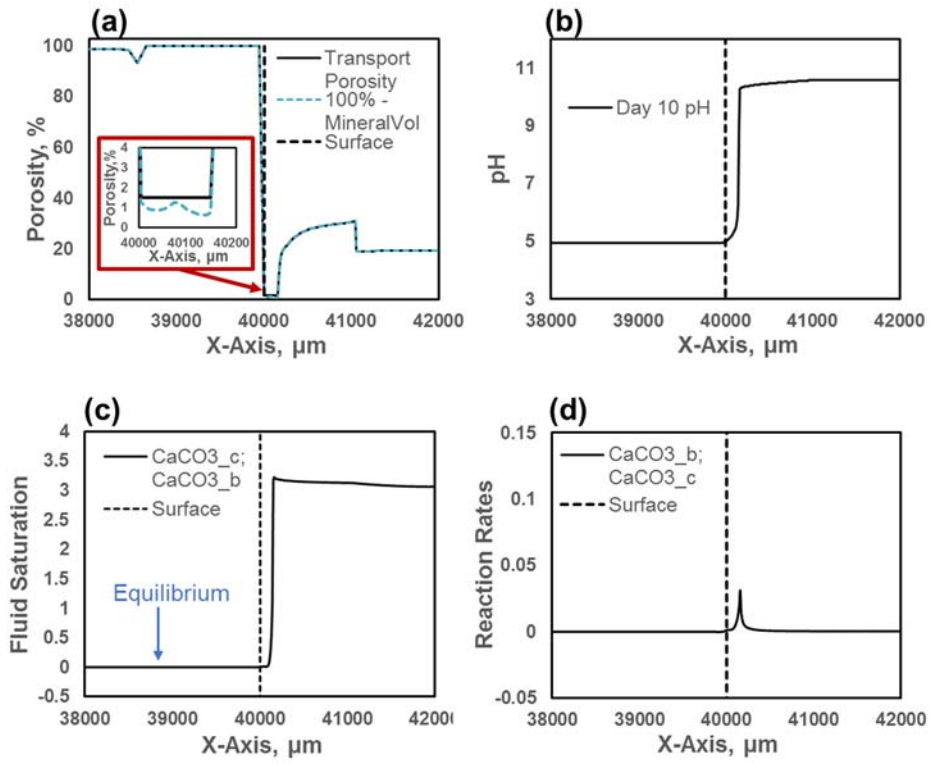

Figure S6 Simulation results for Day 10 with the consideration of nucleation in addition to incomplete filling of nanopores. (a) Porosity profile. The porosity for transport is $\emptyset_{min}$ when $1 - \sum_j \emptyset_{mj} < \emptyset_{min}$, according to Eq. 5. This porosity allows diffusion of the acidic brine through the carbonated layer. (b) pH profile. (c) $CaCO_3$ saturation. The brine saturation is reduced to equilibrium with secondary $CaCO_3$ formed in brine. (d) Reaction rates for $CaCO_3$. $CaCO_3$ is precipitating at the inner front of the carbonated layer, but is not dissolving at the outer front of the carbonate layer.

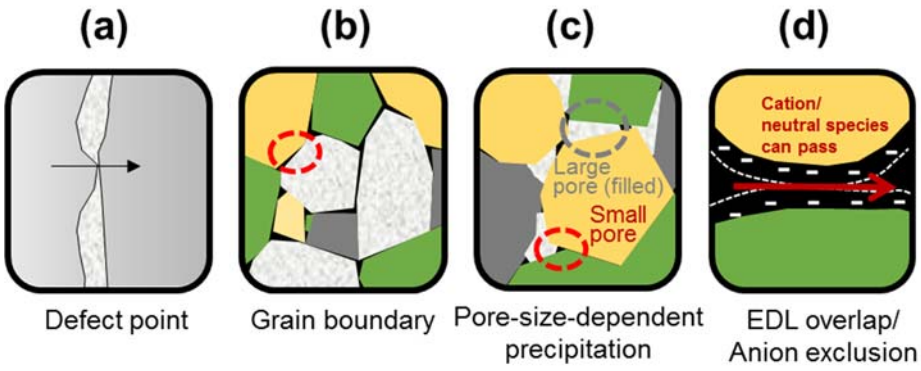

Figure S7. Illustration of possible causes for inefficiency of the carbonated layer in filling all the pore spaces. Arrows and red dotted circles in the figures indicate possible pathways for CO_2.

S4. Discussion of modeling parameters

In the governing equation (Eq. 1), we include a diffusion term and a reaction term for the stagnant system. The diffusion term is fixed during the numerical simulation (m = 2 and $D_i = 3.0 \times 10^{-9}$ m^{-2}/s in Eq. 2), and the reaction kinetics are composed of instantaneous speciation reactions, transition state theory (TST) kinetics for mineral dissolution and growth, and the newly incorporated nucleation kinetics. The spontaneous speciation reaction parameters are database values that are summarized in Table 1. The TST kinetics are adjusted within literature-reported ranges (Table 1). The nucleation kinetics parameters are fixed according to available database values and our experimental measurements (See Section "Nucleation of $CaCO_3$ in Brine"). In addition to these parameters, we have an additional empirical exponent f in Eq. 7, which indicates the degree of dependency of the reaction rate on $1 - \sum_j \emptyset_{mj}$: The larger the f, the greater the dependency. The initial compositions are either known from experiments (for CO_2 pressure and aqueous solution),

or calculated from the XRF data (for the cement domain, as described in Section S2). Because the parameters for the nucleation kinetics and initial domains are from experiments, they are treated as known values and are fixed throughout this work. Below is a discussion on the effects of the diffusivity D_i (in Eq. 2), the cementation exponent m (in Eq. 2), TST kinetics, and secondary C-S-H phases. Because in the TST equation (in Eq. 4) the specific surface area (A_{ss}) and the rate constant (k) are multiplied for rate calculation and there are large reported ranges for both of them, it is not meaningful to analyze them separately, so we consider them as one single parameter $A_{ss} \cdot k$, as listed in Table 1.

Diffusivity D_i and cementation exponent m. As mentioned in the Main Text and listed in Table S2, the diffusivity D_i is in the range of 10^{-9} m^2/s, with $D_i(H^+) > D_i(OH^-) > D_i$(other). The variation of D_i(other) is about 2 times in the relevant temperature range. The activation energy for ion diffusivity in water is about 5 kcal/mol or 21 kJ/mol,[10] resulting in $D_i(95^oC) = 1.6\ D_i(25\ ^oC)$. In the model we assumed $D_i = 3 \times 10^{-9}$ m^2/s, because the result with this D_i value is similar to the results obtained with specified D_i's for the major ions listed in Table S2. Figure S8a plots the results where D_i was reset as 1.5×10^{-9} m^2/s and 6×10^{-9} m^2/s. The effective diffusivity is more dependent on the cementation exponent m than on D_i. Although m values between 1.7 to 4.1 have been observed,[11] the value for m is usually close to 2; for example, m is 1.8–2.0 for consolidated sandstones.[11] Because $m = 2$ is suggested for systems without further information about m,[12] we fixed m at 2 in our model. Figure S8b shows the modeling results with $m = 1.8$ and 2.2.

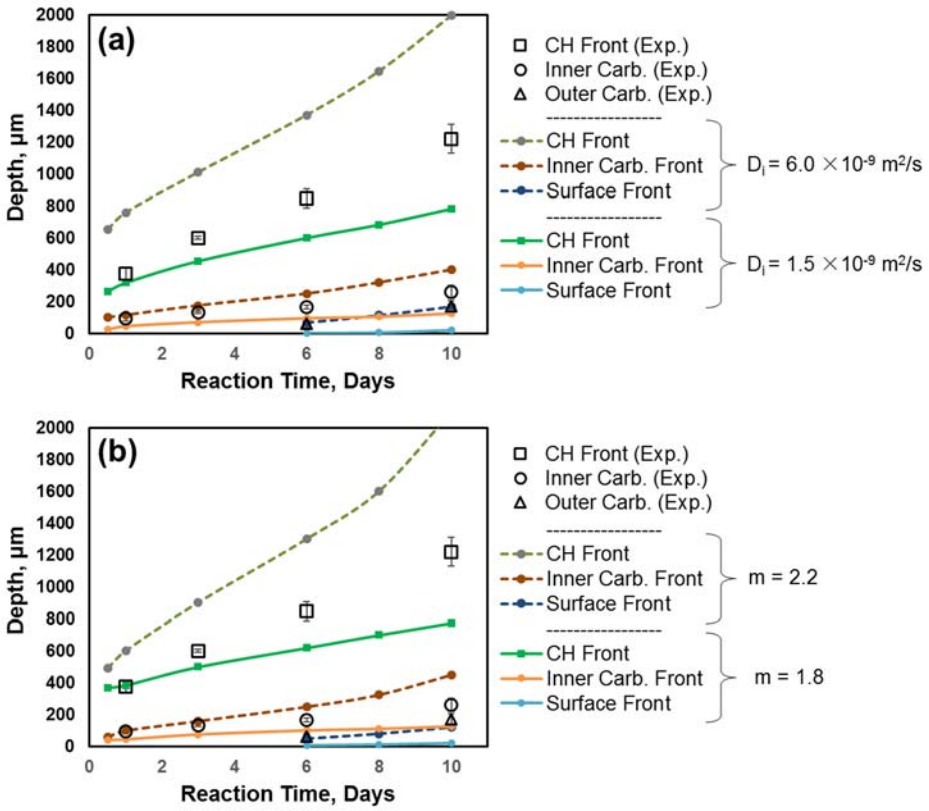

Figure S8. Modeling results with various D_i and m, plotted in (a) and (b), respectively.

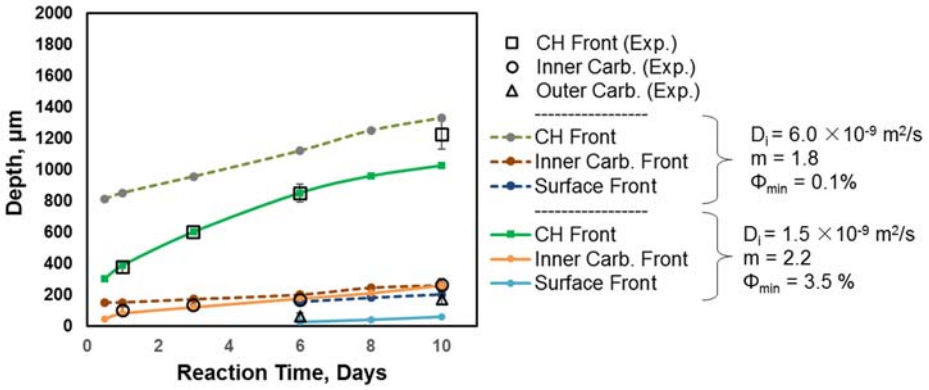

Figure S9. Modeling results for lower and upper bounds of diffusivity.

The minimum porosity of 1.5% is fitted with $D_i = 3 \times 10^{-9}$ m^2/s and $m = 2.0$. If we use $D_i = 1.5 \times 10^{-9}$ m^2/s and $m = 2.2$ for the lower bound of diffusion, the minimum porosity obtained is 0.1%, and if we use $D_i = 6 \times 10^{-9}$ m^2/s and $m = 1.8$ for the upper bound of diffusion, the minimum porosity obtained is 3.5 %. As shown in Figure S9, these two cases do not match well with the experimental results. Therefore, the minimum porosity of 1.5 % from $D_i = 3 \times 10^{-9}$ m^2/s and $m = 2.0$ is arguably more reasonable.

Equations 6 and 7 in the main text define a continuous function to turn off precipitation when the porosity is approaching zero. Such continuity in numerical code is effective in maintaining numerical stability and performance, and thus provides much better performance than discontinuous "switches". The empirical exponent f in Eq. 7 determines the dependency of the reaction rate on $1 - \sum_j \emptyset_{mj}$, as shown in Figure S10. The results for $f = 2 - 4$ do not have an appreciable difference from those shown in Figure 2g-h in the Main Text, and thus are not plotted here.

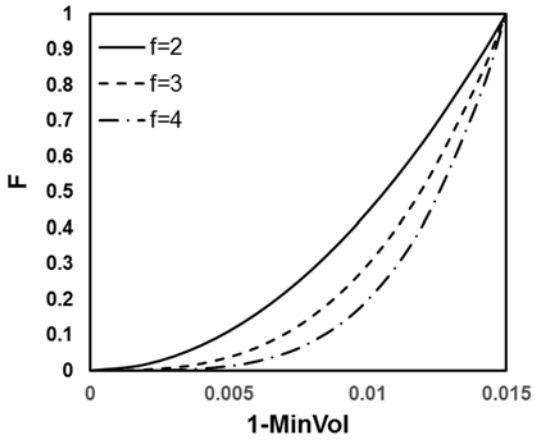

Figure S10. Factor F in Eqs. 6 and 7 as a function of $1 - \sum_j \emptyset_{mj}$.

TST kinetics. The reaction kinetics have an obvious impact on reaction zone propagation. The most important reaction rate is that of calcite, followed by C-S-H, and finally CH. The SiO_2 reaction is so slow in the system that its rate does not have noticeable effects when tuned within a reasonable range. The roles of the primary reactions are shown in Figure S11.

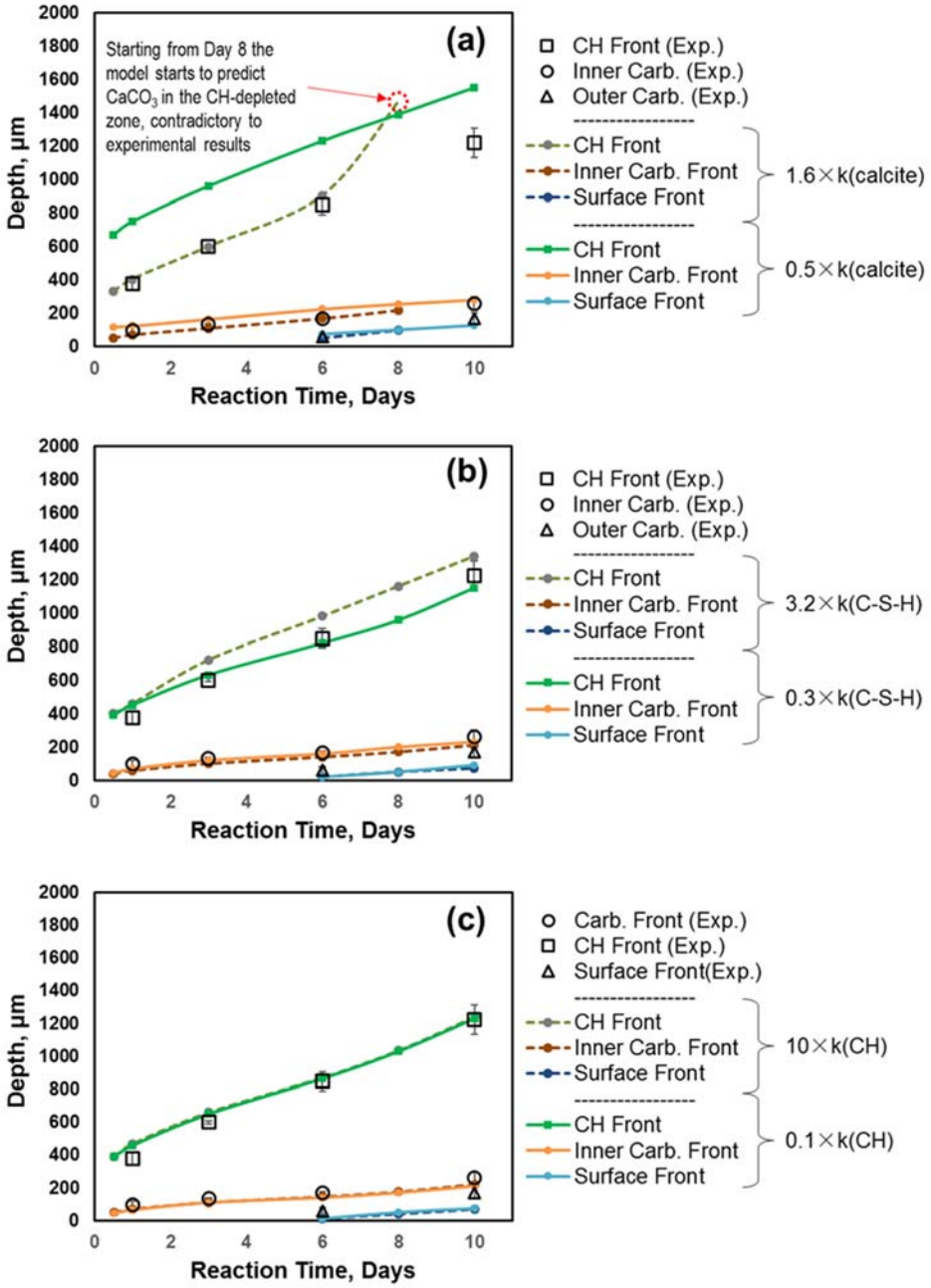

Figure S11. Modeling results with varying TST kinetics. Plots (a), (b), and (c) show results with various kinetics (by weighting the rate constants) for calcite, C-S-H, and CH, respectively.

The presence of two compositions of C-S-H. When the model was first set up, only C-S-H with Ca to Si ratio of 1.6: 1 (called as 1.6) was included. Knowing that C-S-H has a range of Ca to Si ratios, we decided to include a secondary C-S-H phase. Because it is a secondary phase, the Ca-to-Si ratio is expected to be lower because Ca is more leachable than Si. After we introduced C-S-H (0.8) into the model, the modeling results were not significantly different (Figure S12), thus, we decided not to further complicate the system with additional C-S-H phases.

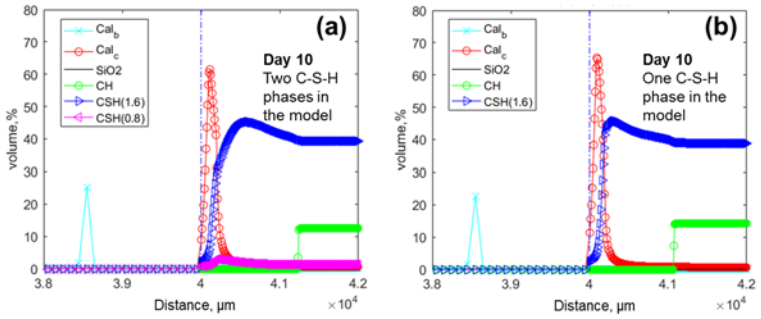

Figure S12. Comparison of modeling results at Day-10 with and without C-S-H (0.8) as secondary C-S-H.

Other considerations. The parameters in the nucleation rates, mainly the interfacial energy and the kinetic factor J_o, were obtained in our previous studies, in which we employed synchrotron-based grazing incidence small angle x-ray scattering to monitor *in situ* $CaCO_3$ precipitation on substrates at nanoscale in aqueous solution.[13-16] Because currently available parameters for nucleation are limited, and many are based on bulk measurement, we used the values obtained from our experiments without further tuning the them. In the reactive transport model, we incorporated heterogeneous nucleation (nucleation on substrate), because in the experiment > 80% of the secondary $CaCO_3$ in

brine was attached on the wall of the Teflon liner in the reactor. Also, heterogeneous nucleation is preferred because its energy barrier (47 mJ/m^2) is much lower than required by homogeneous nucleation (nucleation in solution, interfacial energy ~ 100 mJ/m^2).[10, 14] The grid cells where we added substrate are arbitrary, and their location does not affect the final result as long as nucleation can take place in them. In addition, the liquid-to-solid ratio is another important factor that can affect the modeling result. We fixed this ratio at 16, the value used in our experiments. The sizes of the grid cells could affect modeling results if the discretization is not fine enough. The numerical grids in our model were fine enough to eliminate grid size effects, meaning that results were similar when the grids were refined further.[17] Smaller grid cells produce results similar to those shown in the main text, but they noticeably reduce computational efficiency and lead to long simulation time and difficulty in numerical algorithm. Figure S13 compares the results at Day 1 with the grid cell size specified in the main text and with grid cell size reduced by 50%.

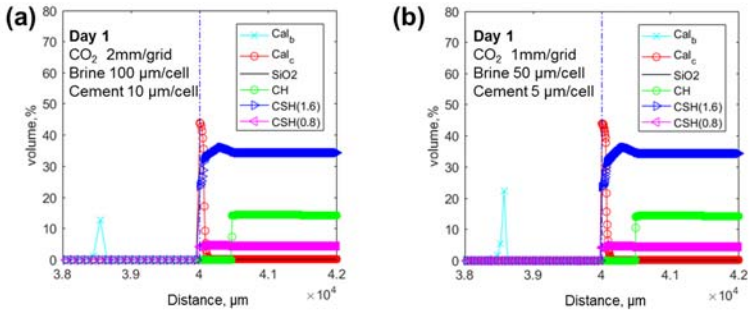

Figure S13. Comparison of modeling results with (a) grid cell sizes specified in the main text and (b) with grid cell sizes reduced by 50%. The profiles of mineral volumes are slightly smoother with finer grid cells but the results are not significantly different.

References

1. De Yoreo, J. J.; Waychunas, G. A.; Jun, Y.-S.; Fernandez-Martinez, A., In Situ Investigations of Carbonate Nucleation on Mineral and Organic Surfaces. *Rev. Mineral. Geochem.* **2013,** *77*, (1), 229-257.

2. Navrotsky, A., Energetic Clues to Pathways to Biomineralization: Precursors, Clusters, and Nanoparticles. *Proc. Natl. Acad. Sci. USA.* **2004,** *101*, (33), 12096-12101.

3. De Yoreo, J., Crystal Nucleation: More than One Pathway. *Nat. Mater.* **2013,** *12*, (4), 284-285.

4. Li, Q.; Lim, Y. M.; Flores, K. M.; Kranjc, K.; Jun, Y.-S., Chemical Reactions of Portland Cement with Aqueous CO_2 and Their Impacts on Cement's Mechanical Properties under CO_2 Sequestration Conditions. *Environ. Sci. Technol.* **2015,** *49*, (10), 5476-5483.

5. Thomas, J.; Jennings, H. Science of Concrete. http://people.ce.gatech.edu/~kk92/hyd07.pdf

6. Poisson, A.; Papaud, A., Diffusion Coefficients of Major Ions in Seawater. *Mar. Chem.* **1983,** *13*, (4), 265-280.

7. Li, Y.-H.; Gregory, S., Diffusion of Ions in Sea Water and in Deep-Sea Sediments. *Geochim. Cosmochim. Acta* **1974,** *38*, (5), 703-714.

8. Brunet, J.-P. L.; Li, L.; Karpyn, Z. T.; Kutchko, B. G.; Strazisar, B.; Bromhal, G., Dynamic Evolution of Cement Composition and Transport Properties under Conditions Relevant to Geological Carbon Sequestration. *Energy Fuels* **2013,** *27*, (8), 4208-4220.

9. Zhang, L.; Dzombak, D. A.; Nakles, D. V.; Brunet, J.-P. L.; Li, L., Reactive Transport Modeling of Interactions between Acid Gas ($CO_2 + H_2S$) and Pozzolan-Amended Wellbore Cement under Geologic Carbon Sequestration Conditions. *Energy Fuels* **2013,** *27*, (11), 6921-6937.

10. Lasaga, A. C., *Kinetic Theory in the Earth Sciences*. Princeton University Press: 1998.

11. Archie, G. E., The Electrical Resistivity Log as an Aid in Determining Some Reservoir Characteristics. *Transactions of the AIME* **1942,** *146*, (01), 54-62.

12. Holzbecher, E., *Environmental Modeling: using MATLAB*. Springer Science & Business Media: 2012.

13. Li, Q. Calcium Carbonate Formation in Energy-Related Subsurface Environments and Engineered Systems. Washington University in St. Louis, 2016.

14. Li, Q.; Fernandez-Martinez, A.; Lee, B.; Waychunas, G. A.; Jun, Y.-S., Interfacial Energies for Heterogeneous Nucleation of Calcium Carbonate on Mica and Quartz. *Environ. Sci. Technol.* **2014,** *48*, (10), 5745-5753.

15. Li, Q.; Jun, Y.-S., Heterogeneous Calcium Carbonate Nucleation in Saline Solution: Thermodynamic and Kinetic Contributions. In *251st ACS National Meeting*, San Diego, USA, 2016.

16. Li, Q.; Jun, Y.-S., Experimental Quantification of the Kinetic Factor in the Nucleation Rate Equation. In *253rd ACS National Meeting*, San Francisco, USA, 2017.

17. Marty, N. C.; Tournassat, C.; Burnol, A.; Giffaut, E.; Gaucher, E. C., Influence of Reaction Kinetics and Mesh Refinement on the Numerical Modelling of Concrete/Clay Interactions. *J. Hydrol.* **2009,** *364*, (1), 58-72.